Self-organization of Tissue Growth by Interfacial Mechanical Interactions in Multi-layered Systems

Tailin Chen[1,4, #], Yan Zhao[3, #], Xinbin Zhao[1], Shukai Li[1], Jialing Cao[1], Jing Du[1,4, *], Yanping Cao[2, *], and Yubo Fan[1,4,5*]

[1] Key Laboratory for Biomechanics and Mechanobiology of Chinese Education Ministry, School of Biological Science and Medical Engineering, Beihang University, Beijing 100191, China

[2] Institute of Biomechanics and Medical Engineering, Department of Mechanical Engineering, School of Aerospace, Tsinghua University, Beijing 100084, China

[3] State Key Laboratory of Advanced Design and Manufacturing for Vehicle Body, College of Mechanical and Vehicle Engineering, Hunan University, Changsha 410082, China

[4] Beijing Advanced Innovation Centre for Biomedical Engineering, Beihang University, Beijing 100191, China

[5] Key Laboratory of Human Motion Analysis and Rehabilitation Technology of the Ministry of Civil Affairs, National Research Center for Rehabilitation Technical Aids, Beijing 100176, China

[#] These authors contributed equally

* Correspondence: dujing@buaa.edu.cn (J.D.), caoyanping@tsinghua.edu.cn (Y.P.C), yubofan@buaa.edu.cn (Y.B.F.)

Abstract

Morphogenesis is a spatially and temporally regulated process involved in various physiological and pathological transformations. In addition to the associated biochemical factors, the physical regulation of morphogenesis has attracted increasing attention. However, the driving force of morphogenesis initiation remains elusive. Here, we show that during the growth of multi-layered tissues, morphogenetic process can be self-organized by the progression of compression gradient stemmed from the interfacial mechanical interactions between layers. In tissues with low fluidity, the compression gradient is progressively strengthened during differential growth between layers and induces stratification through triggering symmetric-to-asymmetric cell division reorientation at the critical tissue size. In tissues with higher fluidity, compression gradient is dynamic and induces 2D in-plane morphogenesis instead of 3D deformation accompanied with cell junction remodeling regulated cell rearrangement. Morphogenesis can be tuned by manipulating tissue fluidity, cell adhesion forces and mechanical properties to influence the progression of compression gradient during the development of cultured cell sheets and chicken embryos. Together, the progression of compression gradient regulated by interfacial mechanical interaction provides a conserved mechanism underlying morphogenesis initiation and size control during tissue growth.

Key words: compression gradient, interfacial interaction, morphogenesis, biomechanics, self-organization, tissue fluidity

Introduction

Morphogenesis is a common process that occurs widely in embryonic development, tissue regeneration and cancer progression. The orchestration of morphogenetic processes is complex and involves spatial and temporal regulation by biochemical factors (e.g., cell polarity signals and morphogen gradient) and physical factors [1-3]. Emerging studies have revealed that proper morphogenesis relies on the mechanical force of the cells and their environment. For example, apical constriction of cells caused by the contractility of myosin [4], cell junction remodeling (called cell intercalation) [5] and tissue stiffness-dependent cell migration [6] have been reported as important mechanisms in tissue shaping during embryonic development. These studies indicate the essential functions of cellular and molecular mechanics in the progression of morphogenesis. However, the upstream events, especially the initial driving forces of morphogenesis, remain unknown.

In complex living systems, tissues are always organized as multi-layered composite construction. The interactions between layers are essential in tissue homeostasis maintenance and morphogenesis during embryonic development and pathological progression [7-9]. The interaction of cancer cells and their adjacent stroma plays a key role in the progression of the diseases, including tumor invasion [10,11]. In addition to biochemical communications, increasing evidence has shown the essential role of physical interactions between adjacent layers in the regulation of morphogenesis [6,12-14]. For instance, follicle formation in chicken embryos is initiated by mechanical forces transduced from the dermal layer to the epidermal layer [15]. The villi of human and chicken guts are formed by the compressive stresses generated by smooth muscle layers on the endoderm and mesenchyme layers [16]. These studies reveal that morphogenesis processes are dependent on the mutual collaboration and mechanical compatibility of

multiple layers. In this sense, it is necessary and important to address the general mechanism underlying the initiation of morphogenesis among various multi-layered tissues.

According to previous studies such as ours and others, differential growth expansion in a film/substrate system may cause biaxial in-plane compression of the film and lead to intriguing surface wrinkling patterns[17-24]. And here, by combining *in vitro* and *in vivo* biological experiments, theoretical analysis and numerical simulations, we report a resembling mechanism underlying the initiation of morphogenesis driven by the progression of compression gradient stemmed from the interfacial mechanical interactions between differential growing tissue layers.

Results

Progressive compression gradient is strengthened in epidermal layer during chicken feather follicle morphogenesis

During the development of avian skin, the feather follicles develop by the stratification of single-layered epidermis [25]. In the *in vitro* culture of chicken skins, we found that the feather primordia emerged at Day 2 in cultured epidermis combined with dermis after isolation from HH30 stage embryos (Figure 1a-c). However, when epidermal cell sheet was isolated and cultured alone (without dermal cell layer), it failed to stratify and no primordium was formed (Figure 1b and c), indicating that the interaction between epidermal and dermal layers is essential for the morphogenetic process of epidermal cell sheet. Moreover, we found that during the evolution of epidermis from monolayer to multilayer, the shapes of epidermal cells showed significant alteration from flat to columnar and correlated with the stages in embryo development and with the increased epidermal cell layer number (Figure 1d and e). The deformation degree of epidermal cells was gradually declined with the increased distance to the primordium center (Figure 1f and g). These experimental observations indicate that in the beginning of follicle morphogenesis, a compression gradient was progressively strengthened in the epidermal cell sheet accompanied with the 3D deformation of epidermis. According to our previous studies about the surface wrinkling pattern formation in a non-living chemical film/substrate composite soft material, the progression of compression gradient could be generated by mismatch deformation between adjacent layers through interfacial mechanical interactions [26,27]. Indeed, it has been reported that during the development of chicken skins, dermal cells form aggregations and compress the

adjacent epidermal cells to form follicle primordium [15,28]. Thus, we hypothesize that the mismatch deformation between epidermal and dermal layers by dermal cell aggregation generates compression gradient through interfacial mechanical interactions and causes stratification of epidermis. However, whether tissue stratification could be triggered by the mechanical interactions between adjacent layers during tissue growth remains elusive.

3D tissue morphogenesis could be self-organized at a critical size in multi-layered system

To study the role of interfacial mechanical interactions between layers in the initiation of tissue morphogenesis, we developed a simple film/substrate system composed of a freely growing monoclonal cell sheet and extracellular matrix (ECM) (Figure 2a). To ensure the emergence of stratification, we chose cells without contact inhibitory properties as the *in vitro* model. During the continuous live imaging, the emergence of a monolayer-to-multilayer transition was stably observed at a critical tissue size (Figure 2a-d). This phenomenon occurred in a wide variety of cell types, and the critical size was relatively constant for a given cell type (Figure 2e), indicating a self-organized mechanism of morphogenesis during cell sheet growth. In addition, similar critical sizes were observed in different types of ECM as well as self-secreted ECM by cells (without pre-coated ECM) (Table S1). The behaviours of individual cells during cell sheet growth prior to the 3D morphogenesis transition were examined using a holographic imaging cytometer. Although the cell proliferation rate was negligibly altered during cell sheet expansion (Supplementary Figure S1a), the average area of individual cells significantly decreased, and the average cell thickness concurrently

increased during cell sheet growth, indicating significant cell deformation (Figure 2f-h). Moreover, the largest cell deformation was observed at the central region of the cell sheet (Figure 2i-l). Since the cell sheet was grown from a single cell (monoclonal culture) and the chemical environment is uniform, the active cell contraction was presumably excluded and this cell deformation behaviour mainly reflected a passive a compression gradient within the cell sheet emerged during cell sheet growth. This phenomenon is consistent with previous reports[29,30].

To investigate the mechanism of compression gradient generation in the cell sheet during growth, we performed theoretical analysis. When the cell sheet is considered as continuum material, interfacial shear stress (ISS) would be generated between the cell sheet and substrate layers during cell proliferation and growth. The direction of which is contrary to the relative motion between them, as illustrated in Figure 3a. Thus, cells in the center region of the colony would bear compression due to ISS when the cell monolayer is growing on the substrate despite that cells at the edge are stretched [30](Figure 3a and Supplementary Mechanical Modelling), consistent with the experimental observations (Figure 2i-l). During cell sheet expansion, the elastic strain energy stored in the cell would also increase. When the elastic strain energy in the cell is small, interfacial normal adhesion would impose restriction on delamination, making the cell monolayer grow in plane. Thus, higher compressive stress would be generated further. When the compressive stress reaches a critical value, elastic strain energy stored in the cell may be greater than the energy needed for the occurrence of the interfacial delamination. In this critical condition, stratification may happen, and the elastic strain energy can be released. Theoretical analysis also gave valid quantitative predictions of experiments. First, theoretical results of the distribution of cell areas agree well with the experimental results (Figure 3b). When the compressive strain reaches a critical

161 value, the elastic strain energy stored in the cells may exceed the energy needed for the
162 occurrence of interfacial delamination. At this critical condition, cell delamination may
163 happen, so that the elastic strain energy can be released (Supplementary Mechanical
164 Modelling). Indeed, we found that during the growth of the cell sheet, amounts of cells
165 in the central region were delaminated from the substrate (Figure 3b). According to the
166 theoretical analysis, the critical size of the cell sheet for 3D morphogenesis depends on
167 mechanical properties of cell sheet and substrate and interactions between them. This
168 is confirmed by finite element simulations which well resembled the morphogenesis at
169 the cell sheet center and also indicated that, when the compressive strain exceeded the
170 critical value, alterations in the cell-substrate interactions could significantly affect the
171 compression gradient during cell sheet growth (Figure 3d and Supplementary
172 Mechanical Modelling). Moreover, experimentally manipulating cell-substrate
173 interactions using the integrin inhibitor RGD significantly attenuated the compression
174 gradient and morphogenesis (Figure 3e-g). In addition, inhibition of the contractility of
175 the cell sheet using the cytoskeleton inhibitor blebbistatin or myosin shRNA
176 significantly attenuated the compression gradient and morphogenesis (Figure 3e-g and
177 Supplementary Figure S2). Based on the theoretical analysis, adhesion between cells
178 may also affect the cell sheet stress. Consistently, inhibition of the cell-cell adhesion
179 force by an E-cadherin neutralizing antibody also reduced the maximum compressive
180 strain in the cell monolayer and inhibited the morphogenetic process (Figure 3e-g).
181 These results show that the emergent 3D morphogenesis of a cell sheet/substrate system
182 could be physically triggered by interfacial mechanical interactions between adjacent
183 layers during growth.
184

Cell division reorientation induces tissue stratification at critical compression condition

We proceeded to investigate the biological mechanism of the cell layer number increase in the central region of the cell sheet induced by cell layer/substrate interfacial interaction. We found that, in contrast to symmetric (parallel) cell division in the peripheral region of large cell colonies, abundant asymmetric (oblique or perpendicular) cell division was observed in the central cells which bore significant compressive strains (Figure 4a-f). Moreover, the orientation of the division plane was closely correlated with cell thickness (Figure 4f). This asymmetric cell division ultimately led at least one daughter cell to locate at the top layer of the cell sheet (Figure 4g and Supplementary Movies 1 and 2). The cell division reorientation was also confirmed by the subcellular localization of the nuclear-mitotic apparatus protein (NuMA), which is involved in the orchestration of mitotic spindle positioning [31] (Figure 4h). Moreover, spindle-rocking experiments indicate that cells in the central region showed a significantly higher level of metaphase plate oscillations which is always associated with asymmetric cell division [32] (Figure 4i). These results indicate that cell division reorientation from symmetric to asymmetric accompanied with compression gradient promotes tissue stratification.

Tissue fluidity controls 2D/3D morphogenetic transition by regulating compression gradient progression

Our experimental results show that the critical sizes of cell sheets for emergent 3D morphogenesis show large variations among different cell types. Notably, some cell types, such as Madin-Darby canine kidney (MDCK) cells, did not display stratification

during our observations (Figure 2e).To further investigate the intrinsic properties of tissue layers that affect the emergent morphogenesis, we compared cell behaviors during cell sheet growth between HeLa and MDCK cells. First, in order to exclude the influence of contact inhibition on MDCK, we conducted statistics on MDCK density. The density of monolayer MDCK cells during our observation is below $1\cdot 10^5$ μm^2, which is far less than the density for contact inhibition of MDCK cells ($2\cdot 10^6$ μm^2) according to the previous study[29]. Moreover, in our results, MDCK cell sheet did not show contact inhibition as shown in our Supplemental Figure S1b and d. We found that, instead of 3D morphogenesis, MDCK cell sheet showed dramatic alterations in its in-plane shape during cell proliferation, with dynamically organized protrusions at cell sheet edges, indicating an emergent 2D morphogenesis (Figure 5a). While few differences in the proliferation rate were observed between these two cell types (Supplementary Figure S1a and b), cell sheet expansion rates showed large variations, being significantly higher in MDCK cells than in HeLa cells (Supplementary Figure S1c and d). In contrast with the HeLa cell sheet behavior, the MDCK cell sheet did not show progressive compression gradient strengthen during growth (Figure 5b and Supplementary Figure S2). Moreover, while the individual cell area in the HeLa cell sheet was relatively steady, MDCK cells exhibited strong area fluctuation during cell sheet growth (Figure 6a and b). Particle imaging velocimetry (PIV) analysis showed that during cell sheet expansion, MDCK cells displayed rapid collective cellular motion with a higher overall cell velocity (root-mean-square, rms velocity, v_{rms}), indicating a fluid-like state [33]. In contrast, the collective behavior of HeLa cells showed slower cell motion, indicating a relatively solid-like state (Figure 6c, d and Supplementary Movie 3). The fluidity of these two cell types was further confirmed by the cell shape index p_0, the median ratio of the perimeter to the square root area of the cells. According to

234 the vertex model, if the cell shape index of the system increases to $p^*_0 \approx 3.81$, a
235 transition from a jammed, solid-like state to an unjammed, fluid-like state occurs [34].
236 Over the course of cell sheet growth, the average cell shape index of MDCK cells was
237 constantly above 3.81, whereas HeLa cells approached the jamming threshold p^*_0
238 (Figure 6e and f). Moreover, the cell shape index was lower in the central region than
239 in the peripheral region of the HeLa cell sheet (Supplementary Figure S4). At the edges
240 of MDCK cell sheet, especially during the formation of protrusions, significant
241 collective cell migration (Figure 5a and Supplementary Movie 4) and abundant cell
242 intercalations such as T1 transitions and rosettes formation were observed (Figure 7a
243 and b). Cell Intercalation is reported as a mechanism for driving tissue extension in
244 embryonic development [35] and could be controlled by external constraints acting on the
245 tissue [36]. In our experiment, most of cell intercalation was observed in cells win
246 relatively smaller areas (less than 300 μm^2), indicating a high level of compressive stain
247 (Figure 7c). Moreover, the cell junction remodeling during intercalation process was
248 closely correlated with the deformation of cell sheet, indicated by the small angles
249 between new junctions and tissue protrusion directions (Figure 7d) and higher tissue
250 elongation rate at the direction of new junctions (Figure 7e). To investigate the effect
251 of the tissue fluidity on the 2D/3D morphogenetic transition, cellular migration ability
252 was inhibited using the small GTPase Rac1 inhibitor NSC23766 [37]. The results showed
253 that Rac1 inhibitor treatment significantly reduced tissue fluidity (Figure 7f and g and
254 Supplementary Movie 5) and induced higher level of compressive strain in MDCK cell
255 sheet (Figure 7h and i), which finally triggered 3D morphogenesis (Figure 7j). In
256 comparison, inhibition of Rho-associated, coiled-coil containing protein kinase (ROCK)
257 by Y27632 slightly enhanced tissue fluidity of MDCK cells (Figure 7f and g and
258 Supplementary Movie 5) and had little effect on morphogenesis (Figure 7h-j). These

results suggest that higher level of tissue fluidity may facilitate the release of the compressive strain generated by the interfacial shear stress between adjacent layers through in-plane cell motion.

Progression of compression gradient contributes to epidermal cell stratification during chicken skin development

Asymmetric cell division is a common mechanism involved in tissue stratification and cell fate differentiation during embryogenesis and cancer progression [38,39]. There is evidence that during the development of chicken skins, the deformation of basement membrane between epidermis and dermis by the aggregation of dermal cells plays crucial role for the initiation of follicle primordium formation [15,28]. According to our results, tissue stratification could be initiated by the mechanical interaction at interface between adjacent layers through compression gradient which is accompanied by cell division reorientation. Thus, we proceeded to verify whether this mechanism is applied to the stratification of epidermis during chicken feather follicle morphogenesis. First, we compared the cell division orientation of the epidermis in single-layered stage and multi-layered stage during skin development. We found that when epidermis was stratified, most of the mitotic spindles of epidermal cells were reoriented from symmetric to asymmetric and closely correlated with cell deformation degree (Figure 8a-c). Moreover, reinforcing the progression of compression gradient by reducing tissue fluidity using Rac1 inhibitor significantly promoted epidermis stratification and follicle formation, indicated by the epidermal cell layer number and pattern geometry of follicle primordium (Figure 8d-i). Reducing tissue fluidity also increased the nuclear localization of β-catenin protein, indicating the promotion of follicle cell fate

determination (Figure 8h and i). In addition, disrupting the interfacial mechanical interaction between epidermal and dermal layers by inhibiting epidermal cell/base membrane adhesion using integrin inhibitor also attenuated the morphogenesis of primordium (Supplementary Figure S5). Thus, our findings suggest a model for the initiation of epidermis stratification during feather follicle formation that dermal cell aggregation induces mismatch deformation between epidermal layer and basement membrane which generates progressive compression gradient in epidermal layer accompanied with cell division reorientation and finally leads to epidermis stratification.

Discussion

In this work, we propose a self-organization mechanism for the initiation of morphogenesis during tissue growth in which a progressive compression gradient caused by emergent macroscopic mechanical stress drives the initiation of morphogenesis at certain developing stages in multi-layered tissues. Our experiments and theoretical analysis show that interfacial mechanical interaction stemmed from mismatch deformation between adjacent layers induces progression of compression gradient which triggers cell delamination and cell division reorientation in solid-like state tissues and ultimately induces 3D deformation and tissue stratification. Meanwhile, in fluid-like state tissues, the interaction between adjacent layers induced dynamic progression gradient leading to 2D tissue deformation instead of 3D deformation (Figure 8j). We also describe the crucial role of progressive compression gradient in epidermis generated by the interaction between epidermal and dermal layers in the initiation of epidermal cell stratification during chicken skin development. Interestingly, in zebrafish embryos, the friction force between mesoderm and neurectoderm layers during cell moving has been reported to be a key determinant in the positioning of neural anlage [40]. Thus, interfacial mechanical interaction between adjacent layers may be a conserved force origin during embryonic development.

Morphogenetic processes always occur at certain developmental stages during tissue growth. During Drosophila wing disc development, different cell proliferation rates induce mechanical stress to shape tissues and control tissue size by regulating proliferation and division orientation [41,42]. In our experimental model, 2D and 3D morphogenetic process emerges at the critical tissue size, which is determined by the critical value of the compressive strain generated by interfacial interaction during tissue

growth. This macroscopic mechanical dissipation provides a possible regulatory mechanism for the spatiotemporal control of morphogenesis and size control of growing tissues. It has been recognized that overcrowding is a common phenomenon in physiological and pathological processes and has a crucial influence on tissue homeostasis maintenance [43,44]. According to our results, critical compressive strain has profound effects on cell behaviors, including cell delamination, cell division reorientation and in-plane cell rearrangement, which all contribute to tissue shaping, homeostasis maintenance and size control. Moreover, in our model experiment, the interfacial shear stress induced compression gradient is autonomously generated by tissue growth and therefore can well simulate the *in vivo* overcrowding conditions with the controlled crowding levels.

Fluidity (jamming/unjamming state) is an important characteristic of tissues and is determined by collective cell motion [45]. Moreover, fluidity is dynamically altered during tissue growth and plays crucial roles in homeostasis maintenance and tumor invasion [33,46,47]. Recently, Saadaoui *et al.* reported that myosin contractility-induced global tissue flow contributed to morphogenesis during avian gastrulation [48]. In our work, we found that tissue fluidity could affect the local accumulation of compressive strain under interfacial interaction between adjacent layers, which finally regulates tissue deformation patterns (2D or 3D). These findings may provide insights into the regulatory mechanism underlying morphogenesis by tissue fluidity.

There is no doubt that mechanical forces play essential roles in the regulation of morphogenesis. The role of cell-scale forces generated by cytoskeleton contraction and transmitted by cell adhesions has been intensively studied in regulating tissue morphogenesis [3]. However, the upstream regulation mechanism of these molecular machines, especially at the tissue scale, is rarely investigated. Our results reveal that

progression of compression gradient controlled by the tissue-scale interfacial shear stress has propounding effects on local cell delamination, reorientation of division plane and cell intercalation to initiate morphogenesis. Moreover, this interfacial shear stress could be stemmed from mismatch deformation during cell migration, aggregation, proliferation, *etc.* Thus, this scale-spanning mechanical loop from the cell scale to the tissue scale and then returns to the cell scale may be a fundamental self-organized mechanism during morphogenetic process in growing multi-layered tissues. Further study is needed to elucidate the molecular mechanotransduction mechanism underlying the regulation of these cell behaviors by the progression of compression gradient under interfacial mechanical interactions.

Taken together, our findings unveil a self-organized mechanism that drives the initiation of morphogenesis in growing multi-layered tissues. These results also open up a new avenue that tissue-scale forces regulate cell behaviours, which could in turn facilitate tissue self-organization.

Materials and Methods

Cell culture and Immunofluorescence

Hela human cervical carcinoma cell、Madin-Darby canine kidney (MDCK) cells、MDA-MB-231 human breast cancer cell、U2OS human osteosarcoma cell were cultured in DMEM medium (containing with 4.5 g/L glucose, L-glutamine, and sodium pyruvate) supplemented with 10% FBS (Life technologies, CA, USA), and 100 IU/mg penicillin-streptomycin (Life technologies, CA, USA) and 1 % (v/v) NEAA (Life technologies, CA, USA). The cells were planted in very sparse concentrations, about 10 cells in a 35mm petri dish, and then individual cells would grow into clones. For the experimental treatment, we use clones of cells grown for the same amount of time. The pharmacological agents were added including Blebbistatin (sigma, 25 μM), RGD (Abcam, 50 μg/ml), E-cadherin neutralizing antibody (Biolegend, 10 μg/ml), NSC23766 (Abmole, 20 μM), Y27632 (Abmole, 20 μM) if applicable. Images were taken on the Nikon microscope. Cells were grown at 37 °C in an incubator with 5% CO_2. Cells grown on glass bottom dishes were fixed with 4% paraformaldehyde for 10 min at room temperature. Incubate the cells with 5% BSA, in PBST (PBS+0.1% Tween 20) for 2 hours. Cells were incubated with primary antibodies at the optimal concentrations (according to the manufacturer's instructions) at 4 °C overnight. After washing, cells were incubated for 2 hours with secondary antibodies: 488/568/633 IgG (H+L) and/or Alexa Flour 568/647 phalloidin (Invitrogen) for 1 hour. Cell nucleus were stained with DAPI (4',6-diamidino-2-phenylindole, Invitrogen) for 10 min at room

temperature. Confocal images were taken on the Leica microscope equipped with a 10x, 40x or 63x objective. Experiments were replicated at least three times.

Live imaging

Live cell imaging was performed in Leica microscope or HoloMonitor M4, enclosed in an incubator to maintain the samples at 37 °C and 5% of CO_2 throughout the experiments. Images were acquired every 10 min with Leica software. Spindle-rocking experiments were acquired every 3 min with Leica microscope. HoloMonitor M4 is a Quantitative phase imaging-based cell analyzer utilizing the principle of digital holographic microscopy. Live cell imaging was performed in HoloMonitor M4, enclosed in an incubator to maintain the samples at 37 °C and 5% of CO_2 throughout the experiments. Images were acquired every 10 min with HStudio 2.7.

PIV (Particle Image Velocimetry) Measurement

PIV analysis was conducted using a custom algorithm based on the MatPIV software package for MATLAB (Figure 6c,6d,6f,7e and 7g.). We used a series of live cell images of HeLa and MDCK to calculate the velocity of the cells in the cell sheet. The mean velocity was subtracted from calculated velocity fields to avoid any drift-related bias and to get the velocity fields of the cells. The heat maps of magnitude are also exported subtracting the mean velocity. From the exported text files, we measured the overall cell speed, or root-mean-square (rms) velocity vrms and calculated the average vrms of each type of cell. The correlation algorithm was coded using MATLAB in our lab. Experiments were replicated at least three times.

Image processing and Quantification

Cell data analysis of HoloMonitor M4(Figure 2g,2h,4g and S1): Cell area, cell thickness, cell sheet area and cell sheet thickness were analyzed by the software HStudio 2.7. HStudio 2.7 can automatically segment and extract physical parameters of the cell. For more details, please refer to the official manual.

The area of cell clones and individual cells (Figure 2e,2i,3b,3f,6a and 7i): Cell boundary labeling and areas were determined manually in Fiji.

Cell thickness, width and division angle (Figure 4b and 4f): The collected confocal tomography images were imported into Bitplane imaris for 3D reconstruction. After reconstruction, XZ and YZ profiles were randomly selected to measure thickness, width and cell division angle manually. Data was measured on three samples, using three regions of the image.

Thickness, width and division angle in chicken embryo skin (Figure 1e,1g,8b,8g and 8i): The collected confocal tomography images were imported into Bitplane imaris. Cell thickness, length, and division Angle were measured manually on software.

Pattern geometry in Chicken embryo skin (Figure 8e and 8f): Diameter and spacing was measured manually using Fuji.

Shape index (Figure 6e,6f): To determine the cell boundary, we used a semi-automatic segmentation pipeline. We manually enhanced the blurry boundaries of the cells. After processing the image by binary Ostu, we produced the finally image by Median filtering. We extracted the parameters by image segmentation to obtain the area and perimeter.

Cell trajectory (Figure 6c): The cell tracking image is produced by software Bitplane imaris.

Junctions analyzed (Figure7a 7b 7c 7d and 7e): Cell boundary labeling and areas were determined manually in Fiji[49].

Strain field analysis

The area of each cell was calculated by Fuji software, and the compression strain of each cell was calculated according to Eq (3). Finally, origin software is used to draw the compression strain diagram (Figure 5b).

Embryos、skin culture and immunofluorescence

Fertilized eggs were bought from local farms. The eggs were cultured in a moist environment at 37 °C and staged according to Hamburger and Hamilton[5]. Dorsal skin pieces were dissected from E7 embryos and spread flat on the Polycarbonate membrane (pore size: 0.4 μm, Corning, Cat.No.3413). Make sure that the bottom side is down. Culture is DMEM with 2% chick serum and 10% FBS along with pharmacological agents NSC23766 (Abmole, 20 μM), RGD (Abcam, 100 μg/ml) if applicable. Skin pieces were cultured for 48 hours at 37 °C before being fixed in 4% paraformaldehyde in PBS. Images were taken on the Nikon stereoscopic microscope. Pattern geometry was calculated using Fiji to measure the spacing and diameter. Skin culture details were performed as previously described. For immunofluorescence staining, Embryos or cultured dissected skin pieces were fixed in 4% paraformaldehyde in PBS and embedded in OCT. The tissue blocks were placed in liquid nitrogen for 1 minute and frozen section. The section thickness is about 14 μm. We incubate the sections with 5% BSA, in PBST (PBS+0.1% Tween 20) for 2 hours. The sections were incubated with

primary antibodies at the optimal concentrations (according to the manufacturer's instructions) at 4 °C overnight. After being washed with PBS, the sections were incubated for 2 hours with secondary antibodies: 488/568/633 IgG (H+L) for 1 hour. Nucleus were stained with DAPI (4',6-diamidino-2-phenylindole, Invitrogen) for 10 min at room temperature. Confocal images were taken on the Leica microscope equipped with a 10 x, 40 x or 63 x objective. Experiments were replicated at least three times.

Quantification and Statistical analysis

The number of biological replicates in each experimental result was indicated in the figure legends. Data were presented as means ±SEM. Significance was determined using Student's t test to compare the differences between two experimental groups.

References

1 Nishimura, T. & Takeichi, M. Shroom3-mediated recruitment of Rho kinases to the apical cell junctions regulates epithelial and neuroepithelial planar remodeling. *Development* **135**, 1493-1502, doi:10.1242/dev.019646 (2008).

2 Gallet, A. Hedgehog morphogen: from secretion to reception. *Trends Cell Biol* **21**, 238-246, doi:10.1016/j.tcb.2010.12.005 (2011).

3 Heisenberg, C. P. & Bellaiche, Y. Forces in tissue morphogenesis and patterning. *Cell* **153**, 948-962, doi:10.1016/j.cell.2013.05.008 (2013).

4 Martin, A. C., Kaschube, M. & Wieschaus, E. F. Pulsed contractions of an actin-myosin network drive apical constriction. *Nature* **457**, 495-499, doi:10.1038/nature07522 (2009).

5 Rauzi, M., Lenne, P. F. & Lecuit, T. Planar polarized actomyosin contractile flows control epithelial junction remodelling. *Nature* **468**, 1110-1114, doi:10.1038/nature09566 (2010).

6 Barriga, E. H., Franze, K., Charras, G. & Mayor, R. Tissue stiffening coordinates morphogenesis by triggering collective cell migration in vivo. *Nature* **554**, 523-527, doi:10.1038/nature25742 (2018).

7 Carvalho, L. & Heisenberg, C. P. The yolk syncytial layer in early zebrafish development. *Trends Cell Biol* **20**, 586-592, doi:10.1016/j.tcb.2010.06.009 (2010).

8 Lilly, B. We have contact: endothelial cell-smooth muscle cell interactions. *Physiology (Bethesda)* **29**, 234-241, doi:10.1152/physiol.00047.2013 (2014).

9 Bhowmick, N. A. & Moses, H. L. Tumor-stroma interactions. *Curr Opin Genet Dev* **15**, 97-101, doi:10.1016/j.gde.2004.12.003 (2005).

10 Mueller, M. M. & Fusenig, N. E. Friends or foes - bipolar effects of the tumour stroma in cancer. *Nat Rev Cancer* **4**, 839-849, doi:10.1038/nrc1477 (2004).

11 Gupta, G. P. & Massague, J. Cancer metastasis: building a framework. *Cell* **127**, 679-695, doi:10.1016/j.cell.2006.11.001 (2006).

12 Munster, S. *et al.* Attachment of the blastoderm to the vitelline envelope affects gastrulation of insects. *Nature* **568**, 395-399, doi:10.1038/s41586-019-1044-3 (2019).

13 Bailles, A. *et al.* Genetic induction and mechanochemical propagation of a morphogenetic wave. *Nature* **572**, 467-473, doi:10.1038/s41586-019-1492-9 (2019).

14 Carvalho, L. *et al.* Control of convergent yolk syncytial layer nuclear movement in zebrafish. *Development* **136**, 1305-1315, doi:10.1242/dev.026922 (2009).

15 Shyer, A. E. *et al.* Emergent cellular self-organization and mechanosensation initiate follicle pattern in the avian skin. *Science* **357**, 811-815, doi:10.1126/science.aai7868 (2017).

16 Shyer, A. E. *et al.* Villification: how the gut gets its villi. *Science* **342**, 212-218, doi:10.1126/science.1238842 (2013).

17 Zhao, Y. *et al.* Effect of lateral dimension on the surface wrinkling of a thin film on compliant substrate induced by differential growth/swelling. *Journal of the Mechanics and Physics of Solids* **83**, 129-145, doi:10.1016/j.jmps.2015.06.003 (2015).

18 Audoly, B. & Boudaoud, A. Buckling of a stiff film bound to a compliant substrate-Part III:. Herringbone solutions at large buckling parameter. *Journal of the Mechanics and Physics of Solids* **56**, 2444-2458, doi:10.1016/j.jmps.2008.03.001 (2008).

19 Audoly, B. & Boudaoud, A. Buckling of a stiff film bound to a compliant substrate-Part II:. A global scenario for the formation of herringbone pattern. *Journal of the Mechanics and Physics of Solids* **56**, 2422-2443, doi:10.1016/j.jmps.2008.03.002 (2008).

20 Audoly, B. & Boudaoud, A. Buckling of a stiff film bound to a compliant substrate-Part I:. Formulation, linear stability of cylindrical patterns, secondary bifurcations. *Journal of the Mechanics and Physics of Solids* **56**, 2401-2421, doi:10.1016/j.jmps.2008.03.003 (2008).

21 Bowden, N., Brittain, S., Evans, A. G., Hutchinson, J. W. & Whitesides, G. M. Spontaneous formation of ordered structures in thin films of metals supported on an elastomeric polymer. *Nature* **393**, 146-149, doi:10.1038/30193 (1998).

22 Breid, D. & Crosby, A. J. Surface wrinkling behavior of finite circular plates. *Soft Matter* **5**, 425-431, doi:10.1039/b807820c (2009).

23 Cai, S., Breid, D., Crosby, A. J., Suo, Z. & Hutchinson, J. W. Periodic patterns and energy states of buckled films on compliant substrates. *Journal of the Mechanics and Physics of Solids* **59**, 1094-1114, doi:10.1016/j.jmps.2011.02.001 (2011).

24 Li, B., Cao, Y. P., Feng, X. Q. & Gao, H. Mechanics of morphological instabilities and surface wrinkling in soft materials: A review. *Soft Matter* **8**, 5728-5745, doi:10.1039/c2sm00011c (2012).

25 Mayerson, P. L. & Fallon, J. F. The spatial pattern and temporal sequence in which feather germs arise in the white Leghorn chick embryo. *Dev Biol* **109**, 259-267, doi:10.1016/0012-1606(85)90453-1 (1985).

26 Han, X., Zhao, Y., Cao, Y. & Lu, C. Controlling and prevention of surface wrinkling via size-dependent critical wrinkling strain. *Soft Matter* **11**, 4444-4452, doi:10.1039/c5sm00761e (2015).

27 Zhao, Y. *et al.* Effect of lateral dimension on the surface wrinkling of a thin film on compliant substrate induced by differential growth/swelling. **83**, 129-145 (2015).

28 Ho, W. K. W. *et al.* Feather arrays are patterned by interacting signalling and cell density waves. *PLoS Biol* **17**, e3000132, doi:10.1371/journal.pbio.3000132 (2019).

29 Puliafito, A. *et al.* Collective and single cell behavior in epithelial contact inhibition. *Proceedings of the National Academy of Sciences of the United States of America* **109**, 739-744, doi:10.1073/pnas.1007809109 (2012).

30 Trepat, X. *et al.* Physical forces during collective cell migration. *Nature Physics* **5**, 426-430, doi:10.1038/nphys1269 (2009).
31 Pirovano, L. *et al.* Hexameric NuMA:LGN structures promote multivalent interactions required for planar epithelial divisions. *Nat Commun* **10**, 2208, doi:10.1038/s41467-019-09999-w (2019).
32 Haydar, T. F., Ang, E., Jr. & Rakic, P. Mitotic spindle rotation and mode of cell division in the developing telencephalon. *Proc Natl Acad Sci U S A* **100**, 2890-2895, doi:10.1073/pnas.0437969100 (2003).
33 Garcia, S. *et al.* Physics of active jamming during collective cellular motion in a monolayer. *Proc Natl Acad Sci U S A* **112**, 15314-15319, doi:10.1073/pnas.1510973112 (2015).
34 Bi, D., Lopez, J., Schwarz, J. M. & Manning, M. L. J. N. P. A density-independent rigidity transition in biological tissues. **11**, 1074 (2015).
35 Guillot, C. & Lecuit, T. Mechanics of epithelial tissue homeostasis and morphogenesis. *Science* **340**, 1185-1189, doi:10.1126/science.1235249 (2013).
36 Aigouy, B. *et al.* Cell flow reorients the axis of planar polarity in the wing epithelium of Drosophila. *Cell* **142**, 773-786, doi:10.1016/j.cell.2010.07.042 (2010).
37 Raftopoulou, M. & Hall, A. Cell migration: Rho GTPases lead the way. *Dev Biol* **265**, 23-32, doi:10.1016/j.ydbio.2003.06.003 (2004).
38 Neumuller, R. A. & Knoblich, J. A. Dividing cellular asymmetry: asymmetric cell division and its implications for stem cells and cancer. *Genes Dev* **23**, 2675-2699, doi:10.1101/gad.1850809 (2009).
39 Lechler, T. & Fuchs, E. Asymmetric cell divisions promote stratification and differentiation of mammalian skin. *Nature* **437**, 275-280, doi:10.1038/nature03922 (2005).
40 Smutny, M. *et al.* Friction forces position the neural anlage. *Nat Cell Biol* **19**, 306-317, doi:10.1038/ncb3492 (2017).
41 Legoff, L., Rouault, H. & Lecuit, T. A global pattern of mechanical stress polarizes cell divisions and cell shape in

the growing Drosophila wing disc. *Development* **140**, 4051-4059, doi:10.1242/dev.090878 (2013).

42 Mao, Y. *et al.* Differential proliferation rates generate patterns of mechanical tension that orient tissue growth. *EMBO J* **32**, 2790-2803, doi:10.1038/emboj.2013.197 (2013).

43 Eisenhoffer, G. T. *et al.* Crowding induces live cell extrusion to maintain homeostatic cell numbers in epithelia. *Nature* **484**, 546-549, doi:10.1038/nature10999 (2012).

44 Marinari, E. *et al.* Live-cell delamination counterbalances epithelial growth to limit tissue overcrowding. *Nature* **484**, 542-545, doi:10.1038/nature10984 (2012).

45 Sadati, M., Taheri Qazvini, N., Krishnan, R., Park, C. Y. & Fredberg, J. J. Collective migration and cell jamming. *Differentiation* **86**, 121-125, doi:10.1016/j.diff.2013.02.005 (2013).

46 Miroshnikova, Y. A. *et al.* Adhesion forces and cortical tension couple cell proliferation and differentiation to drive epidermal stratification. *Nat Cell Biol* **20**, 69-80, doi:10.1038/s41556-017-0005-z (2018).

47 Park, J. A., Atia, L., Mitchel, J. A., Fredberg, J. J. & Butler, J. P. Collective migration and cell jamming in asthma, cancer and development. *J Cell Sci* **129**, 3375-3383, doi:10.1242/jcs.187922 (2016).

48 Saadaoui, M., Rocancourt, D., Roussel, J., Corson, F. & Gros, J. A tensile ring drives tissue flows to shape the gastrulating amniote embryo. *Science* **367**, 453-458, doi:10.1126/science.aaw1965 (2020).

49 Firmino, J., Rocancourt, D., Saadaoui, M., Moreau, C. & Gros, J. Cell Division Drives Epithelial Cell Rearrangements during Gastrulation in Chick. *Developmental cell* **36**, 249-261, doi:10.1016/j.devcel.2016.01.007 (2016).

Acknowledgments

General: We thank J. Y. Fu (China Agricultural University) for providing GFP-H2B+ U2OS cells and C. Dong (The Pennsylvania State University) and Y. Liang (EV-bio) for discussions during the preparation of this paper. We also thank S. Wu (China Agricultural University) and X. Liu (Beihang University) for technical support of chicken embryonic experiments and PIV analysis, respectively.

Funding: This work was supported by the National Key R&D Program of China (2017YFA0506500, 2016YFC1102203, and 2016YFC1101100), the National Natural Science Foundation of China (31370018, 11972206, 11902114, 11421202, 11827803, and 11902020), and Fundamental Research Funds for the Central Universities (ZG140S1971).

Author contributions: T.L.C, Y.Z., J.D., Y.P.C, and Y.B.F. designed the study, performed and interpreted experiments. X.B.Z. and S.K.L. helped with cell experiments and statistical analysis. J.L.C helped with PIV analysis. Y.Z. and Y.P.C. did mechanical analysis. J.D., Y.P.C., and Y.B.F. conceived and supervised this project and prepared the paper.

Competing interests: There are no competing interests.

Figures and Tables

Figure 1

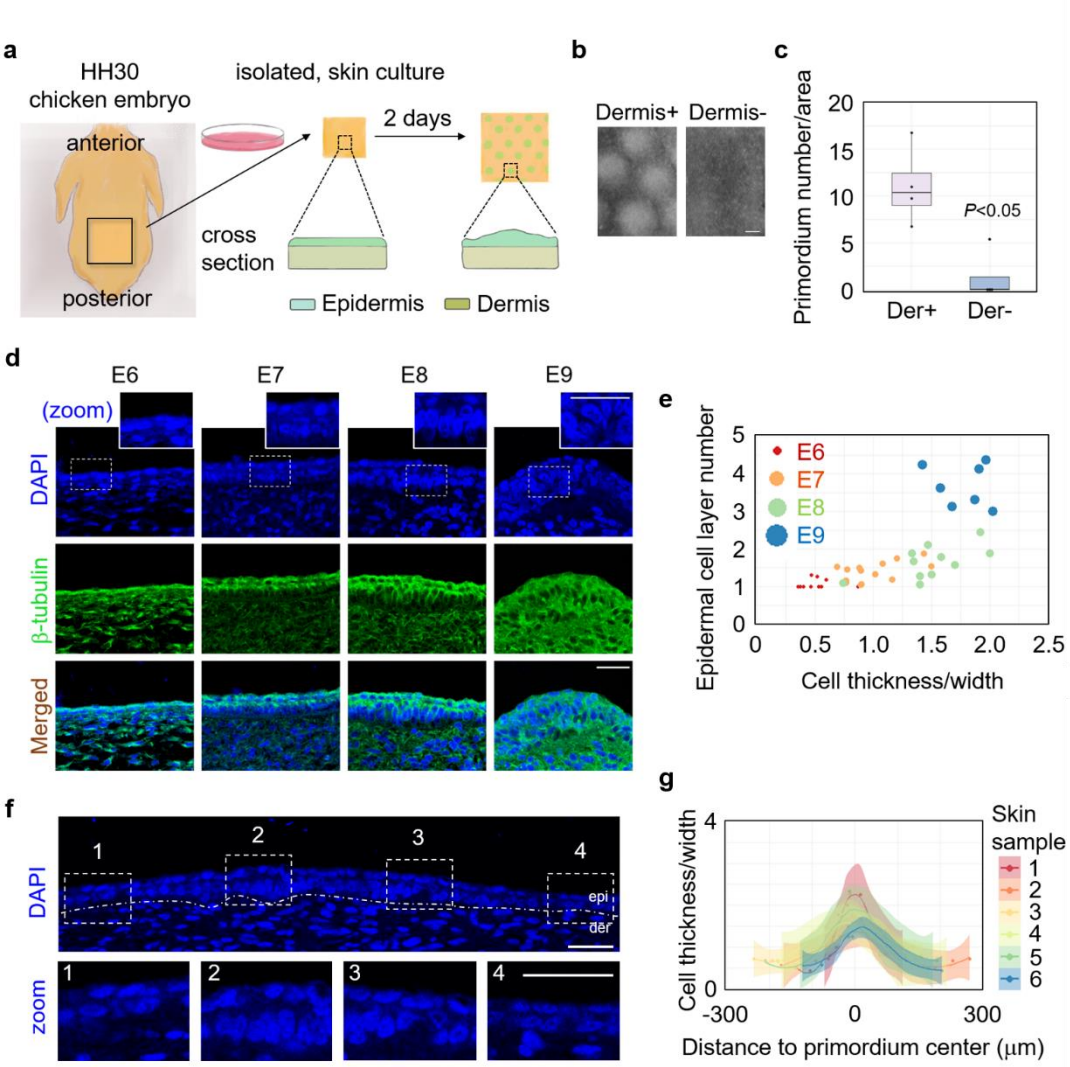

Figure 1. Progressive compression gradient is strengthened in epidermal layer during chicken feather follicle morphogenesis (a) The illustration of experimental workflow for studying the epidermal morphogenesis in cultured chicken skins. (b) *In vitro* culture of embryonic chicken skin with (Der+) or without (Der-) dermal cell layer.

Scale bar: 500 μm. (c) The statistical analysis of primordium number per area (mm^2) in (b). (d) Images of skin tissues from different stages of chicken embryos showing the deformation of epidermal cell shape. Scale bar: 25 μm. (e) The statistical analysis of cell deformation (thickness/width) and cell layer number of epidermis in skin tissues from different stages of chicken embryos. Each dot represents the average value of an embryo. (f) Images of epidermal cell shape deformation at different location around the center of primordium. Scale bar: 25 μm. (g) The statistical analysis of cell deformation (thickness/width) with different distance to the center of primordium.

Figure 2

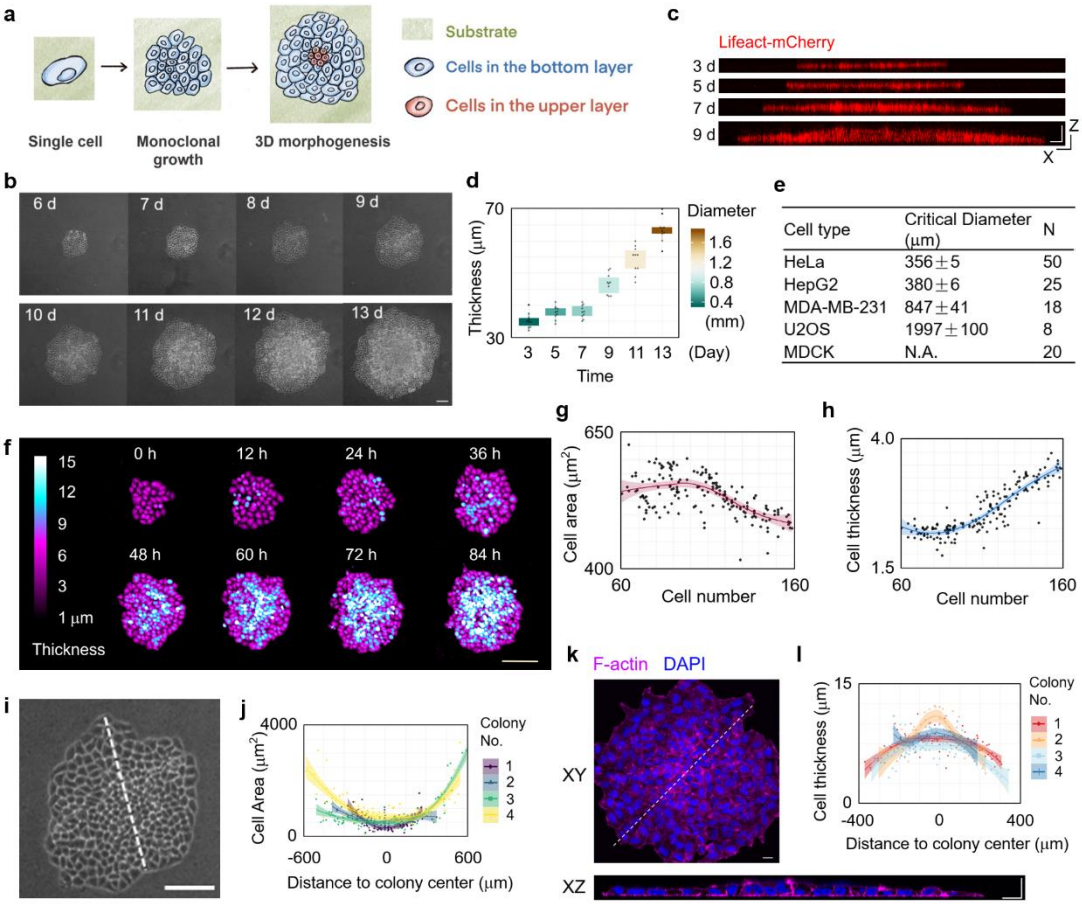

Figure 2. Emergent 3D morphogenesis in a growing monoclonal cell sheet at critical size (a) The illustration of experimental workflow for studying the emergent 3D morphogenesis in a freely growing monolayer Hela cell sheet. (b) Representative phase contrast images of a growing monoclonal Hela cell sheet captured at the indicated time (d: day) after seeding. Scale bar: 100 μm. (c-d) XZ slice images of F-actin indicated by Lifeat-mCherry in a growing monoclonal Lifeat-mCherry^{+} Hela cell sheet captured at the indicated time after seeding. Scale bar: 50 μm. The statistical analysis of cell sheet thickness and diameter of a growing Hela cell sheet. (n = 10). (e) The critical size for 3D morphogenesis of growing cell sheet in different cell types. (f)

The representative live images of a growing Hela cell sheet using HoloMonitor M4 time-lapse cytometer. Scale bar: 150 μm. (g) The statistical analysis of the area of individual cell during Hela cell sheet growth. (h) The statistical analysis of the thickness of individual cell during Hela cell sheet growth. (i) The magnified view of Hela cell sheet at 8 d in (b). Scale bar: 100 μm. (j) The statistical analysis of the individual cell area along the lines in (i). (k) Representative XY and XZ slice images of F-actin and nucleus stained by Phalloidin and DAPI respectively in Hela cell sheet. Scale bar: 20 μm. (l) The statistical analysis of the individual cell thickness along the lines in (i).

Figure 3

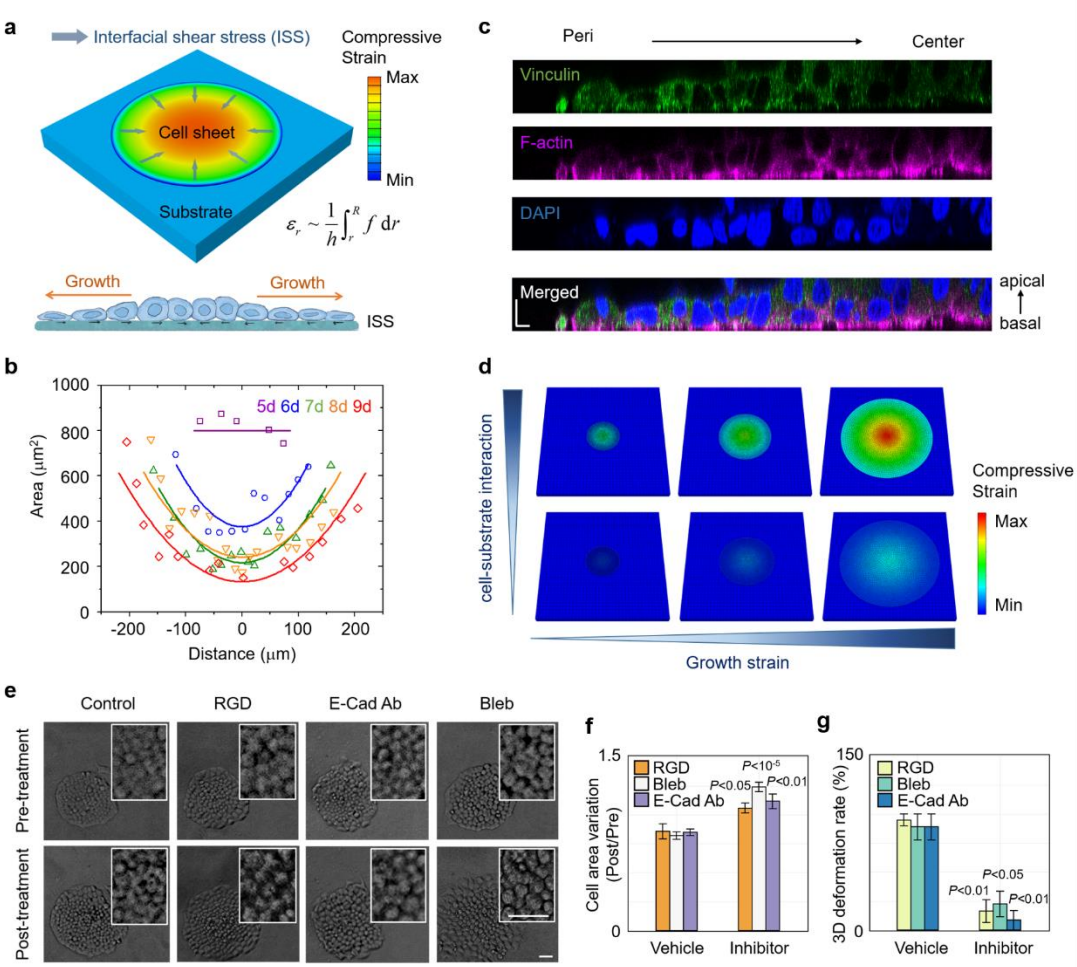

Figure 3. Size-dependent 3D morphogenesis is induced by interfacial shear stress in multi-layered system (a) Theoretical model of a cell monolayer sheet growing on a substrate. f is the interfacial shear stress between the cell sheet and substrate generated by relative motion. h is the thickness of cell sheet. σ_r is the compressive stress in the cell sheet induced by the interfacial shear stress. R is the outer radius of the cell sheet and r is the distance between cell and center of the monolayer sheet. Diagrams of interfacial shear stress between cell and substrate. Direction of interfacial shear stress is contrary to the cell sheet expansion, as the yellow arrow points out. (b) Area of the individual cell along a random line across the center of the cell sheet. Data points refer

to the experimental results and corresponding lines are theoretical predictions obtained by fitting the experimental datas using Eq. 6 in Supplementary Materials. (c) Representative XZ slice image of Vinculin, F-actin and nucleus stained by Vinculin antibody, Phalloidin and DAPI respectively in half of a Hela cell sheet. Scale bar: 10 μm. (d) Finite element simulation of the stress field in the growing cell monolayer with different cell-substrate interactions ($f_{\mathrm{top}} / f_{\mathrm{bottom}} = 5$). Growth strains from left to right are 10%, 60% and 120%, respectively. Color bar shows the distribution of the compressive stress in the cell monolayer. (e) Representative phase contrast images of Hela cell sheet in the presence of inhibitors or vehicle. Scale bar: 50 μm. (f) The statistical analysis of the individual cell area of Hela cell sheet in the presence of inhibitors or vehicle. (n = 10). (g) The morphogenesis percentage of Hela cell sheet in the presence of inhibitors or vehicle. (n = 3).

Figure 4

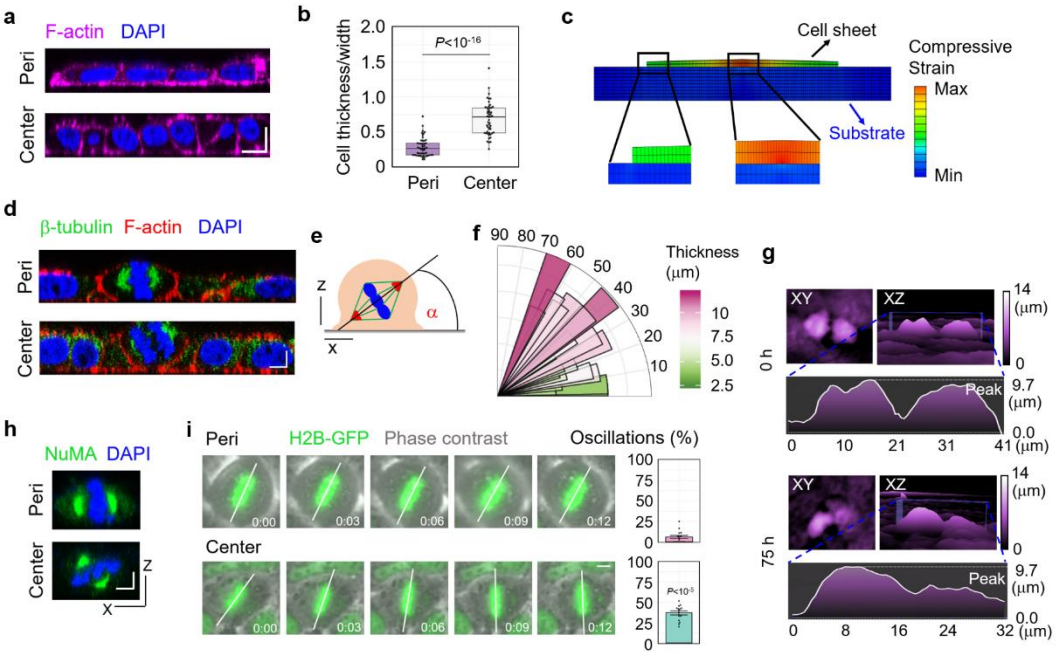

Figure 4. Critical Compression triggers cell division reorientation to induce tissue stratification (a) Representative XZ slice image of F-actin and nucleus stained by Phalloidin and DAPI respectively in the central region and peripheral region of Hela cell sheet. Scale bar: 10 μm. (b) The statistical analysis of cell deformation (thickness/width) in the center region and peripheral region of Hela cell sheet. (n = 50). (c) Cell shape variation induced by interfacial shear stress. (d) Representative XZ slice image of β-tubulin, F-actin and nucleus stained by β-tubulin antibody, Phalloidin and DAPI respectively in the central region and peripheral region of Hela cell sheet. Scale bar: 5 μm. (e) The schematic experimental setting of the mitotic spindle orientation. (f) Distribution of the spindle-axis angles of cells with different thickness in Hela cell sheet. (g) The representative images of dividing cells before (0 h) and after (75 h) critical compression during Hela cell sheet growth using HoloMonitor M4 time-lapse cytometer. (h) Representative XZ slice image of NuMA and nucleus stained by NuMA

antibody and DAPI respectively in the central region and peripheral region of Hela cell sheet. Scale bar: 5 μm. (i) Analysis of spindle oscillation in in the central region and peripheral region of GFP-H2B^{+} U2OS cell sheet. The extent of oscillation was calculated and plotted in bar graphs on the right. Scale bar: 5 μm. (n = 14).

Figure 5

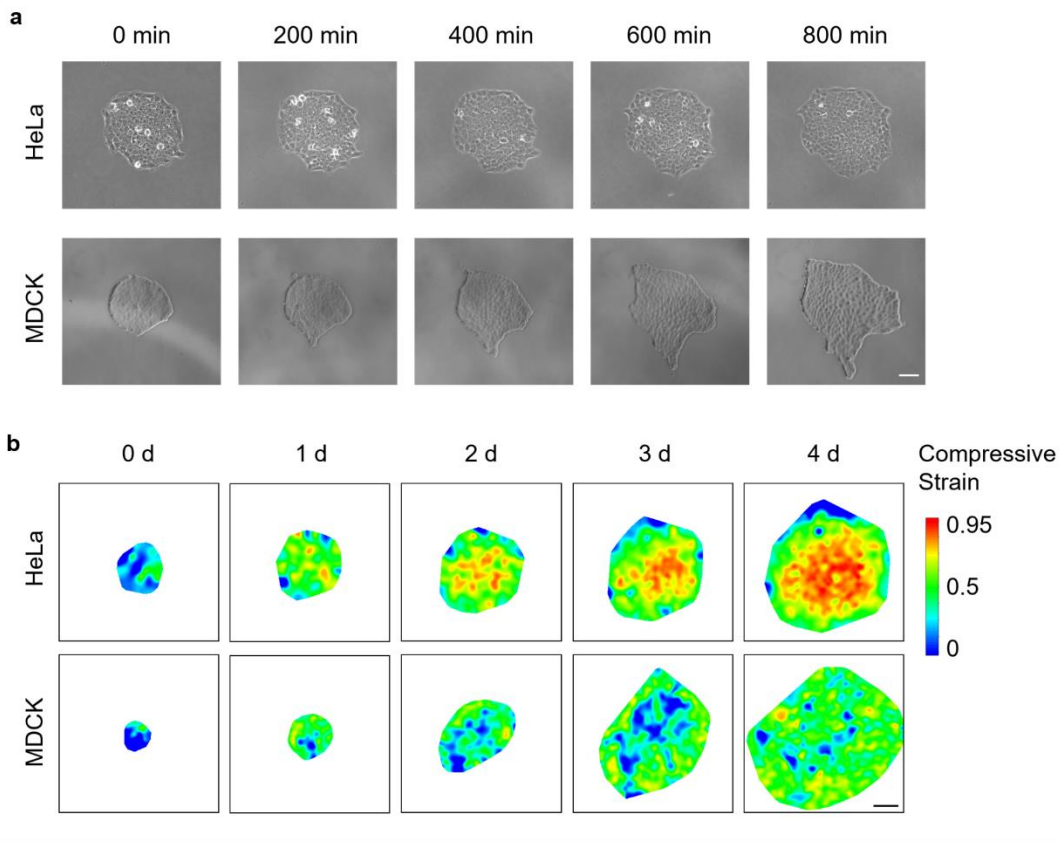

Figure 5. MDCK cell sheet displays 2D deformation during growth (a) Representative phase contrast images of a growing monoclonal MDCK cell sheet captured at the indicated time (min: minute). Scale bar: 100 μm. (b) The calculated strain field evolution during the growth of Hela and MDCK cell sheets at the indicated time (d: day). Scale bar: 100 μm.

Figure 6

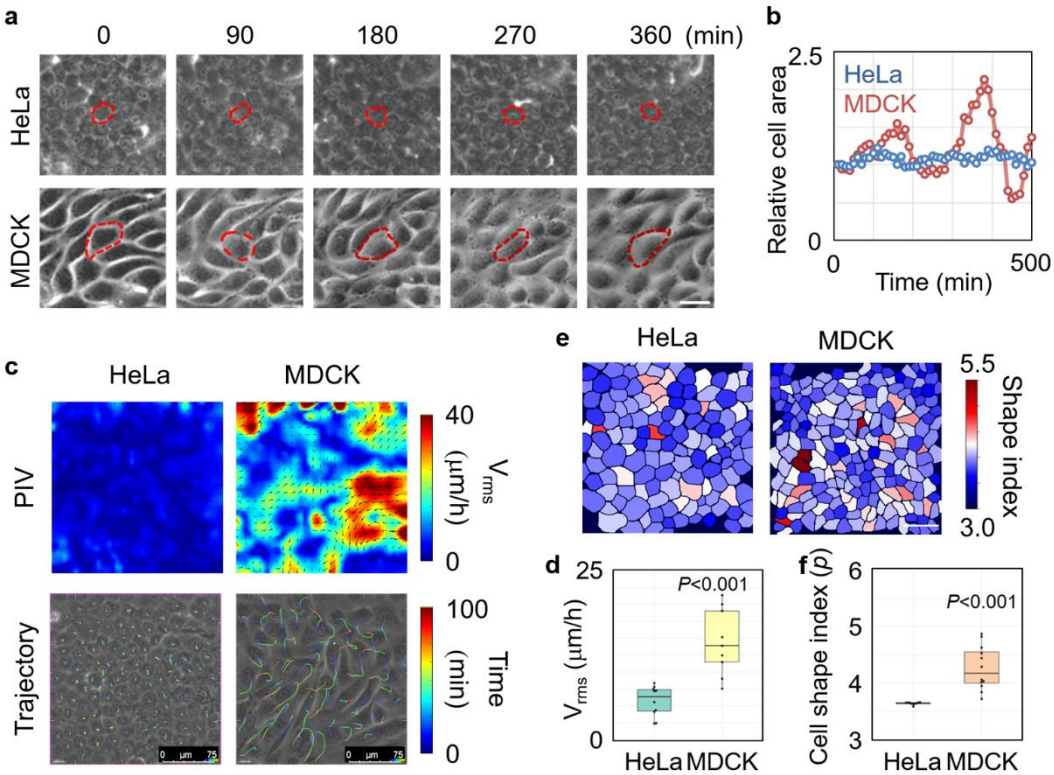

Figure 6. HeLa and MDCK cell sheets show different fluidity during growth (a) The fluctuation of individual cell shape during the growth of Hela and MDCK cell sheets. Scale bar: 25 μm. (b) The area alteration with time of the cell indicated by dotted line in (a). (c) Cell velocity field analyzed by PIV and cell trajectories in Hela and MDCK cell sheets. Scale bar: 75 μm. (d) The statistical analysis of cell speed (rms velocity) measured by PIV in Hela and MDCK cell sheets. (n = 10). (e) The cell shape index distribution of Hela and MDCK cell sheets. Scale bar: 50 μm. (f) The statistical analysis of cell shape index of Hela and MDCK cell sheets. (n = 10).

Figure 7

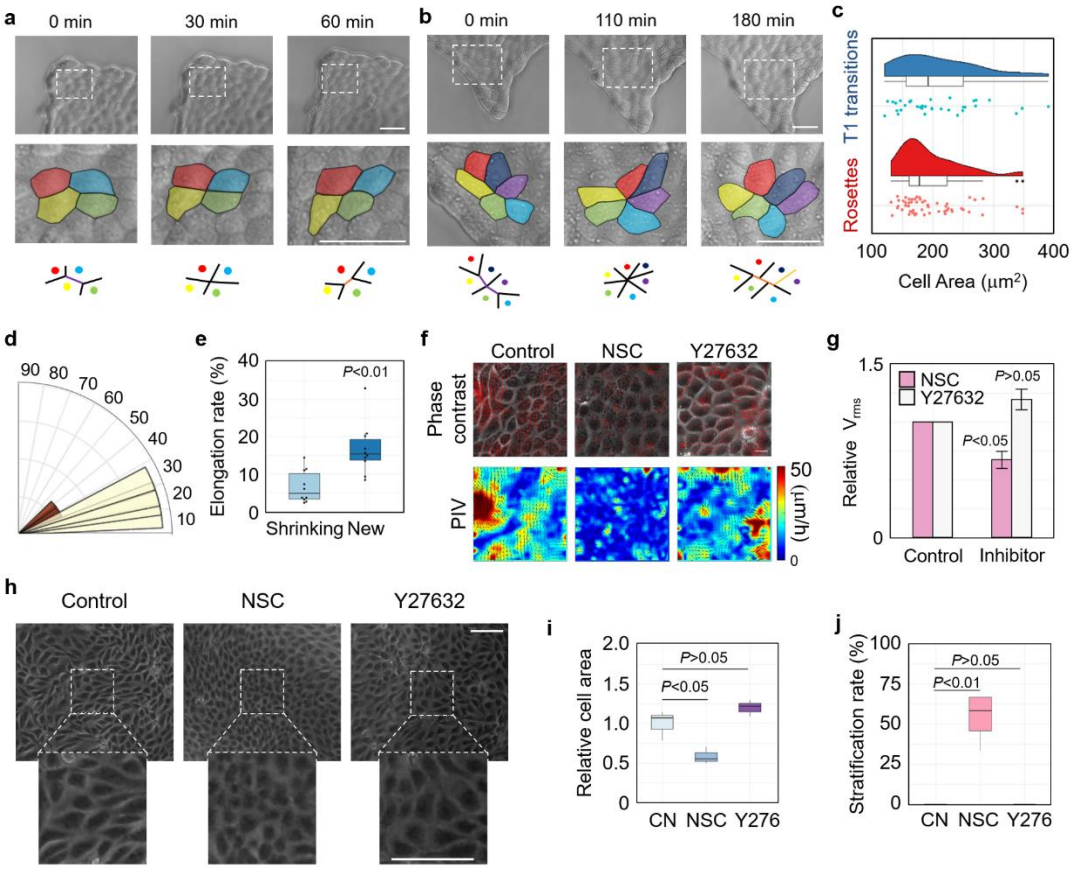

Figure 7. Tissue fluidity controls 2D/3D morphogenetic transition by regulating compression gradient progression (a) Representative image of T1 transition at MDCK cell sheet edges during growth. Cell rearrangements are illustrated at the bottom layer (purple line: shrinking junction, orange line: new junction). (min: minute). Scale bar: 50 μm. (b) Representative image of rosettes at MDCK cell sheet edges during growth. Cell rearrangements are illustrated at the bottom layer (purple line: shrinking junction, orange line: new junction). Scale bar: 50 μm. (c) Cell area distributions of cells be experiencing T1 transitions and rosettes. (d) Distribution of the angles between new junctions and tissue protrusion directions. (e) Cell sheet elongation rate at the

785 direction of shrinking junctions or new junctions. (n = 10). (f) The velocity field
786 superimposed on the corresponding phase contrast (upper panel) and velocity map
787 (lower panel) images measured by PIV of MDCK cell sheet in the presence of inhibitors
788 or vehicle. Scale bar: 20 μm. (g) The statistical analysis of cell speed (rms velocity)
789 measured by PIV of Hela and MDCK cell sheets in the presence of inhibitors or vehicle.
790 (n = 4). (h) Representative phase contrast images of MDCK cell sheet in the presence
791 of inhibitors or vehicle. Scale bar: 100 μm. (i) The statistical analysis of the individual
792 cell area of MDCK cell sheet in the presence of inhibitors or vehicle. (n = 3). (j) The
793 stratification percentage of MDCK cell sheet in the presence of inhibitors or vehicle. (n
794 = 4).
795

Figure 8

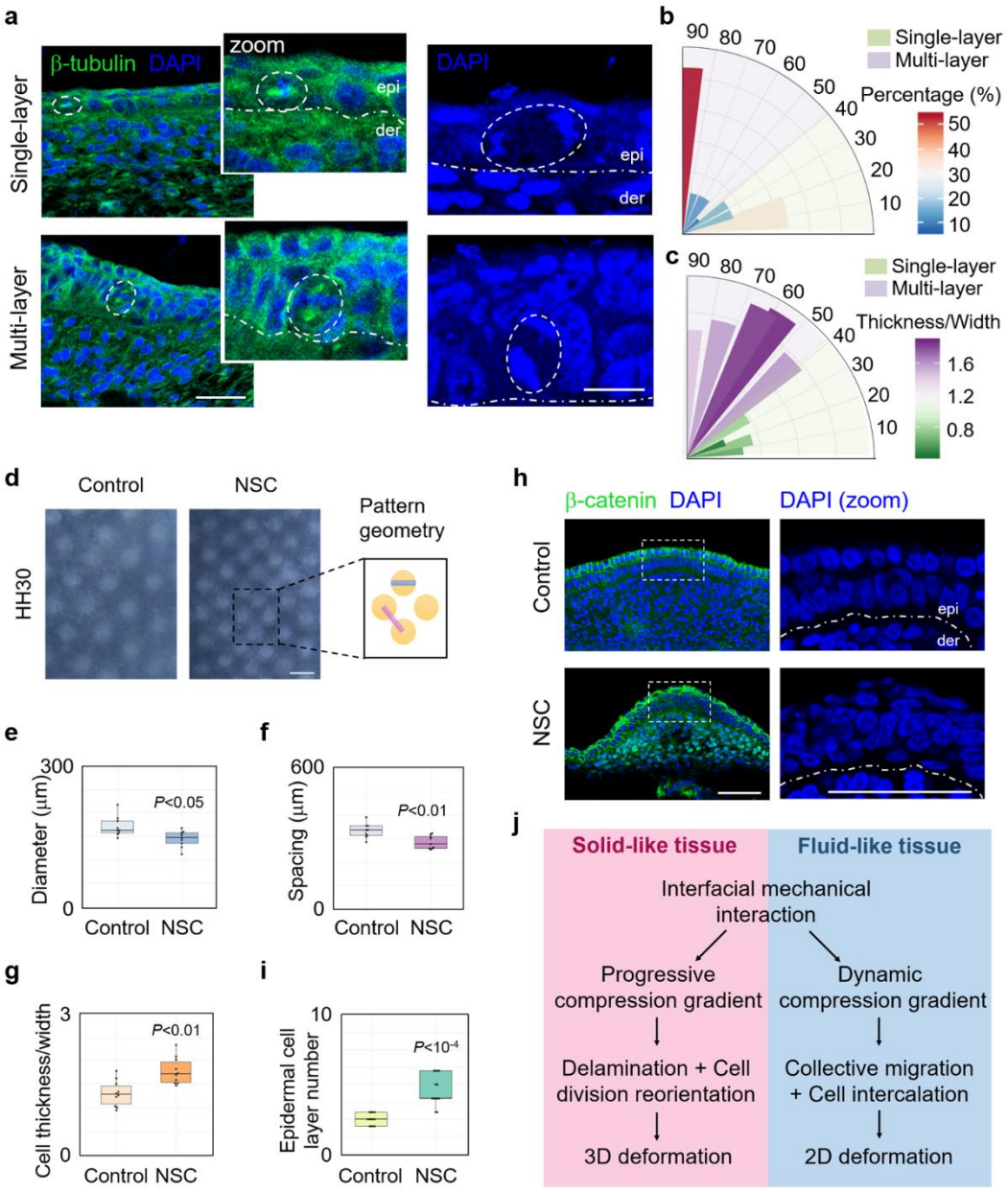

Figure 8. Progression of compression gradient contributes to epidermal cell stratification during chicken skin development (a) Images of embryonic chicken skin showing the orientation of mitoses relative to the basement membrane (white dotted line) in the magnified images (zoom), separating epidermis (epi) from dermis

(der). White dotted circles indicate the mitotic cells in metaphase (left) and anaphase (right). DAPI marks the DNA and β-tubulin antibody immunofluorescence staining marks the spindle. Scale bar: 10 μm. (b) Distribution of the spindle-axis angles of cells in single-layered or multi-layered epithelia of embryonic chicken skin. (c) Distribution of the spindle-axis angles of cells with different cell deformation (thickness/width) in single-layered or multi-layered epithelia of embryonic chicken skin. (d) Reconstitution culture of embryonic chicken skin with or without NSC23766 (NSC). Scale bar: 500 μm. Quantification of (e) spacing and (f) diameter as pattern geometry parameters as illustrated in the right panel of (d). (n = 10). (g) Quantification of cell deformation of epidermis in in the presence of NSC or vehicle. (n = 10). (h) Representative cross section image of β-catenin and nucleus stained by β-catenin antibody and DAPI respectively in reconstitution cultured embryonic chicken skin with or without NSC23766 (NSC). Scale bar: 50 μm. (i) Quantification of layer number of epidermis in (h). (n = 14). (j) Model of 2D and 3D morphogenesis controlled by the interfacial mechanical interactions in multi-layered systems with different tissue fluidity.

Supplementary Materials

Theory model

The theoretical model is shown in Fig. 3a. The cell monolayer is modeled as a thin film, which is attached on the surface of a rigid substrate. Direction of the tangential adhesion force between the cell and substrate is contrary to the relative motion. Thus, compression would be induced when the cell monolayer is growing on the substrate. The tangential adhesion force is assumed as $f = f(r)$, where r is the distance between the cell and the c of the monolayer. f is concerned with the tangential adhesion between the cell and substrate, which is related to the cell type, stiffness of substrate and the rate of cell division or growth. By analyzing the stress state of the monolayer and solving the equilibrium equation, one can obtain the distribution of the equi-biaxial compressive stress in the monolayer

$$\sigma_r = \frac{1}{h}\int_r^R f \, \mathrm{d}r \tag{1}$$

Here R is the outer radius of the cell monolayer, and h is the thickness of cell sheet. The compressive strain can be obtained by the constitutive relation as

$$\varepsilon_r = \frac{1-\nu}{Eh}\sigma_r \tag{2}$$

where E, ν are the modulus and Poisson's ratio, respectively. The central region of the monolayer would sustain higher level of compression than the cells in other regions. Thus, cell extrusion is most likely to occur in the central region, which is consistent with the experimental observations. The maximum compressive strain in the cells can

be obtained as

$$\varepsilon_{\max} = \frac{1-\nu}{Eh}\int_0^R f \, \mathrm{d}r \tag{3}$$

which depends on the cell-substrate interactions and area of the cell monolayer. Based on Eq. (2), one can also obtain the cell area

$$A/A_0 = (1-\varepsilon)^2 \tag{4}$$

where A_0 is the normal area of a full-grown cell without sustaining compression. Eq. (4) demonstrates that distribution of cell area can reflect the strain state in the cell monolayer. With cell proliferation, radius of the cell monolayer increases, and area of cells in the central region is reduced, indicating that the cell monolayer has a high level of compression in the central region.

Given the distribution of the interfacial adhesion force, one can obtain the distribution of the compressive strain and cell area of the cell monolayer. In this work, the tangential adhesion force is assumed to be uniform over the cell monolayer. Thus, the maximum compressive strain in the cell and the distribution of the cell area can be given by

$$\varepsilon_{\max} = \frac{1-\nu}{Eh} fR \tag{5}$$

$$A/A_0 = \left[1 - \frac{1-\nu}{Eh} f(r-R)\right]^2 \tag{6}$$

Based on Eq. (4), distribution of the compressive strains in the Hela cells in experiments can be obtained by analyzing the distribution of cell area, which is shown in Fig. 2b. The sequence in Fig. 2b shows the morphologies of growing Hela cells with the distribution of the compressive strains given in Fig. 5b. The size of the cell monolayer sheet grows bigger along with the cell proliferation, generating higher level of compressive stress in the monolayer. Areas of individual cells in the central region are

reduced due to the increased compressive strains. The experimental observations and calculations are consistent with the theoretical predictions.

To validate the theoretical model, finite element simulations are performed to explore the relation between the cell-substrate interactions and stress field in growing cells. Results of finite element simulations are shown in Fig. 3d. In the finite element model, the growing cell monolayer sheet was placed on a stiff substrate with the interfacial fraction factor being controlled. The cell sheet was under isotropic expansion to simulate the growth. More than 12,000 linear hexahedral elements were adopted to in the simulations. The cell sheet was modeled as the linear elastic material. With the increase of the growth strain, compressive stresses in the cell monolayer are generated due to the cell-substrate interactions, and the central region has a higher level of compressive stress. The stress level can be reduced by regulating the cell-substrate interactions (Fig. 3d). Finite element simulations are consistent with experimental observation and theoretical analysis.

The elastic strain energy stored in the cell would also increase with the cell proliferation. When the elastic strain energy in the cell is small, interfacial normal adhesion would impose restriction on cell extrusion, making the cell monolayer grow in plane. Thus, higher compressive stress would be generated further. When the compressive stress reaches a critical value, elastic strain energy stored in the cell may be greater than the energy needed for the occurrence of the interfacial delamination. In this critical condition, cell extrusion may happen, and the elastic strain energy can be released. The critical condition for the cell extrusion can be written as

$$\gamma A = \frac{E}{1-\nu}\varepsilon_{\max}^{2} V \tag{7}$$

The left hand and right hand of the equation refer to the energy for the interfacial delamination and elastic strain energy in the cell, respectively. γ is the energy per area

for the interfacial delamination, which is related to the interfacial normal adhesion between the cell and substrate. $\varepsilon_{\max}$ is the maximum strain in the cell, and V is the cell volume. Eq. (6) demonstrates that there exists a critical area or size of the cell monolayer at the critical condition of cell extrusion. The critical size of the cell monolayer sheet depends on the mechanical properties of cell and cell-substrate interactions. The cell extrusion can be controlled by regulating the modulus of the cell and cell-substrate interactions.

When the normal adhesion between the cell monolayer and the substrate is enhanced, cell extrusion would be more difficult to happen, and the cell would bear larger compression before extrusion. When the tangential adhesion is larger, higher level of compression would be induced, and the cell extrusion is more likely to happen. The adhesion between the cells may have effect on the cell sheet stress. Maximum compressive stress in the cell monolayer may be reduced when lowering down the adhesion between the cells. Thus, cell extrusion would be more difficult to happen. Cytoskeleton is the main components that determine the cell mechanics. The cytoskeleton can bear compressive stress and store elastic strain energy. If the cytoskeleton in the cell is suppressed, cell extrusion is hard to happen. These predictions were confirmed by experiments (Fig. 3e-g).

Shape of the cell can be changed due to the compression induced by the interfacial shear stress. Thus, the orientation of the cell division may be altered. During the evolution of the cell monolayer sheet, cell shape in the central region was changed from flat to columnar due to the high level of compression stress. While in the periphery of the monolayer, cell shape maintained flat. Stretch ratio of the cell in the direction of thickness can be written as

$$\lambda = 1 + \frac{2\nu}{1-\nu}\varepsilon_r \tag{8}$$

Base on the stretch ratio in Eq. (8), cell thickness/width characterizing cell shape can be obtained as

$$\frac{h}{b} = \frac{\lambda}{1-\varepsilon_r}\frac{h_0}{b_0} \tag{9}$$

Here h and b refer to the cell thickness and width. h_0 and b_0 refer to the initial thickness and width of the cell without sustaining compression. In the periphery of the monolayer, cell thickness/width is small since the compressive strain in the cell is small. While in the central region with high level of compressive strain, cell thickness/width can be very large. This phenomenon of cell shape variation induced by the interfacial mechanical interaction is also confirmed by the finite element simulations, as shown in Fig. 4c.

Supplementary Figures

Supplementary Figure S1

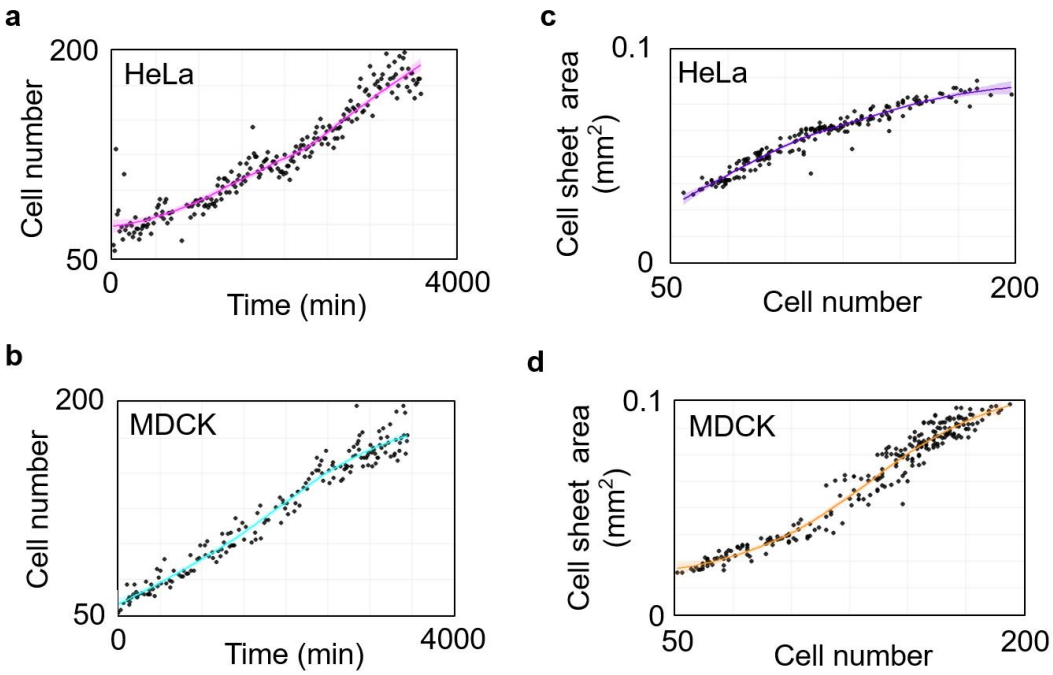

Figure S1. Proliferation and expansion of cell sheets during growth. The statistical analysis of the cell number during Hela cell sheet (a) and MDCK cell sheet (b) growth. The statistical analysis of the cell sheet area during Hela cell sheet (c) and MDCK cell sheet (d) growth.

Supplementary Figure S2

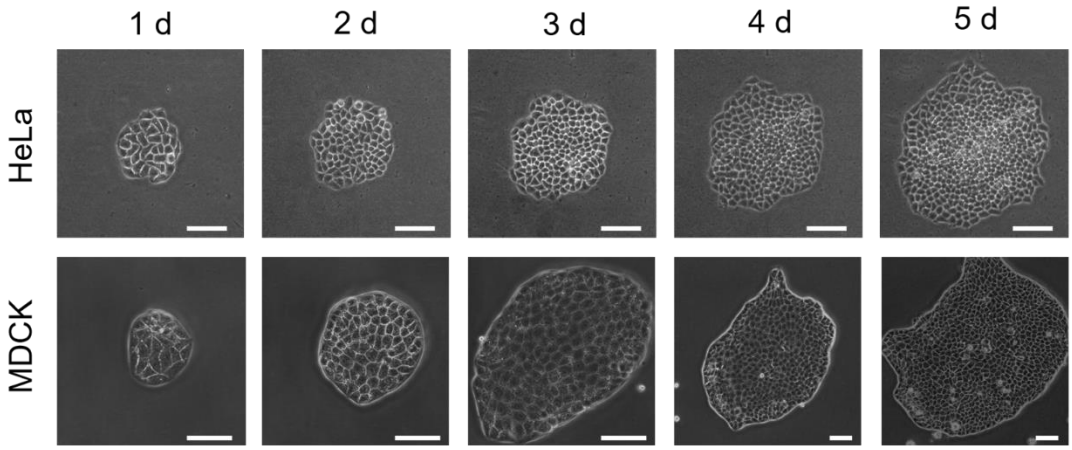

Figure S2. Cell shape alteration during cell sheet growth Representative phase contrast images of a growing monoclonal Hela cell sheet and MDCK cell sheet captured at the indicated time after seeding (d: day). Scale bar: 100 μm.

Supplementary Figure S3

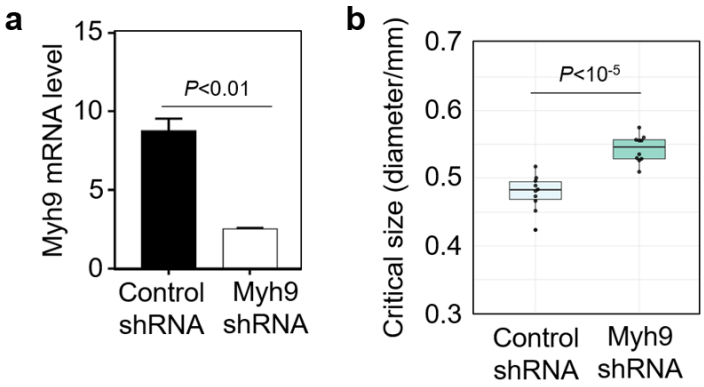

Figure S3. Inhibition of Myosin effects the emergence of 3D morphogenesis (a) The mRNA level of myosin heavy chain 9 gene (myh9) in Hela cells transfected with myh9 shRNA and control shRNA. (n = 3). (b) The critical sizes for morphogenesis in myh9 shRNA cells and control cells. (n = 10).

Supplementary Figure S4

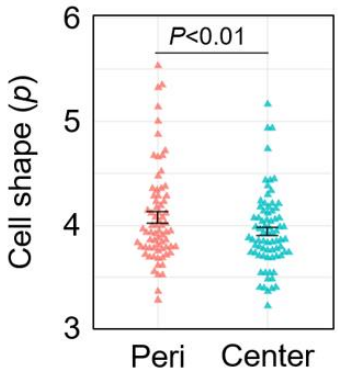

Figure S4. Cell shape index in the peripheral and central regions of HeLa cell sheet

The statistical analysis of cell shape index of cells in the peripheral region and central region of Hela cell sheet. (n = 75).

Supplementary Figure S5

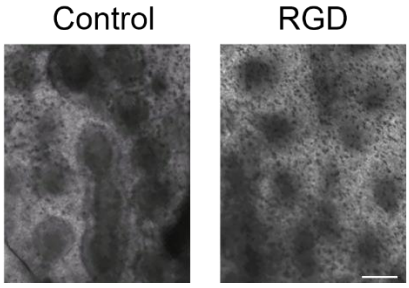

Figure S5. Disrupting the interfacial mechanical interaction between epidermal and dermal layers attenuated the morphogenesis of primordium Reconstitution culture of embryonic chicken skin with or without RGD. Scale bar: 500 μm.

Supplementary Table

ECM type	Critical diameter(μm)	N
No pre-coating ECM	463.8±18.9	10
Collagen	520.3±21.8	10
Fibronectin	493.8±23.9	10
Gelatin	489.1±19.8	10

Table S1. The critical size for 3D morphogenesis of growing cell sheet on different types of ECM.

Supplementary Movies

Supplementary Movie 1. Symmetric cell division before critical compression during Hela cell sheet growth visualized by HoloMonitor M4 time-lapse cytometer.

Supplementary Movie 2. Asymmetric cell division after critical compression during Hela cell sheet growth visualized by HoloMonitor M4 time-lapse cytometer.

Supplementary Movie 3. PIV analysis during Hela and MDCK cell sheets growth.

Supplementary Movie 4. Time-lapse imaging of MDCK cell sheet during growth.

Supplementary Movie 5. PIV analysis during MDCK cell sheet growth in the presence of inhibitors or vehicle (control).